İSTANBUL UNIVERSITY CERRAHPAŞA

ORIGINAL ARTICLE
Electrica 2024; 24(1): 193-200

Improving the Calibration by Power Balancing in Truncated Singular Value Decomposition for Wide-Band Scattering Parameter Data

Semih Doğu

Department of Electronics and Communication Engineering, Istanbul Technical University Faculty of Electrical and Electronics Engineering, Istanbul, Turkey

Cite this article as: S. Doğu, "Improving the calibration by power balancing in truncated singular value decomposition for wide-band scattering parameter data," *Electrica*, 24(1), 193-200, 2024.

ABSTRACT

The field of microwave and millimeter-wave imaging systems is experiencing significant growth in research, primarily attributed to their versatile interaction capabilities with various materials. In the course of image reconstruction, the inverse scattering problem is resolved through either qualitative or quantitative means. The inverse scattering problem can be resolved by utilizing the truncated singular value decomposition (TSVD) algorithm, which is a suitable inversion method that can be employed when there is a need to discard a portion of data. The utilization of multi-frequency multi-static inversion techniques yields results that exhibit greater robustness and clarity when contrasted with single-frequency mono/bi-static configurations. However, it should be noted that the TSVD formulation may not be sufficient in practical experimental situations, as it fails to account for potential deviations in power among excitations at varying frequencies. As a result, it is imperative to perform a calibration process to standardize the power variations across different frequencies. The proposal outlines a calibration methodology that aims to achieve power equilibrium across various frequencies and facilitate the automation of imaging algorithms. The proposed calibration technique is evaluated and demonstrated through the use of a through-the-wall experiment.

***Index Terms*—**Calibration, microwave Imaging, truncated singular value decomposition, wide-band measurements

Corresponding author:
Semih Doğu

E-mail:
dogu16@itu.edu.tr

Received: July 07, 2023

Revision Requested: September 4, 2023

Last Revision Received: November 20, 2023

Accepted: December 20, 2023

Publication Date: January 31, 2024

DOI: 10.5152/electrica.2024.23089

I. INTRODUCTION

Microwave and millimeter-wave imaging systems (MMWIS) are a rapidly expanding field of research due to their ability to interact with many different materials [1]. This feature allows them to be successfully employed in various applications in through-the-wall imaging (TWI), medical imaging, subsurface imaging, and security scanning and tracking [2–15]. During the process of image reconstruction in MMWIS, the inverse scattering problem is solved either qualitatively or quantitatively. In quantitative approaches, the contrast function, which holds the electrical properties of the materials, is aimed at being retrieved [16, 17]. On the other hand, qualitative counterparts seek an indicator that is related to the contrast function, provides faster reconstructions, and only finds the shape of the objects [18–20].

When it is necessary to disregard a specific part of data, the truncated singular value decomposition (TSVD) algorithm can be utilized as an appropriate inversion method in microwave and millimeter wave imaging applications. The selection of the truncated data is mostly determined by the singular values of the input data, and depending on the type of application, this selection becomes crucial. For illustration, in TWI setups, the contribution coming from the wall itself must be truncated. On the other hand, in medical applications, this truncation operation may cause important data loss while reducing the noise effects due to noise, and the target (especially in the first stage of the anomaly) may have similar signal levels. The TSVD is generally employed to find the solution to the inverse microwave scattering problem. For instance, experimental imaging of 3D brain stroke detection is proposed in [21], an angular super-resolution technique is presented for adverse weather aircraft radar in [22], and a TWI application is examined for different versions of TSVD methods in [3]. In [23], it is demonstrated that TSVD is a suitable method for stabilizing the source inversion to improve the inversion capabilities. In addition to solving the inverse problem examples, in [24], TSVD is utilized as an auxiliary technique to reduce the noise in medical images, and in [25], misfit errors and uncertainties from noise in the Laplace domain is reduced via TSVD.

Both qualitative and quantitative approaches suffer from the ill-posedness of the inverse scattering problem, and since the number of measurements is limited and mostly performed outside of the investigated region, constructing a well-posed problem becomes very challenging. The non-linearity can be overcome by the qualitative methods by using a simpler model, yet the problem still stays ill-posed, and they can only provide an estimate of a target's shape. Another issue in the microwave imaging area is the discrepancy between the configurations of actual measurements and the modeled simulation. To tackle this issue, calibration algorithms, either with simulations, measurements, or algorithms, are developed. For instance, a phaseless parametric inversion technique for system calibration for a specific application is presented in [26]. A hybrid calibration technique employing both simulations and measurements is proposed in [27], a calibration technique by averaging 2 consecutive measurements is proposed in [28], and further, a calibration involving a full-wave simulation is given in [29] for real-time brain stroke monitoring. In [30], the calibration between each different frequency is performed by comparing a simulation and an additional measurement done in front of a copper plate. In [3], a calibration procedure is proposed by employing reconstructions at each operating frequency without taking any additional simulations or measurements. In [3], a reconstruction is heuristically selected, and calibration parameters for the rest of the frequencies are calculated according to this fixed frequency. Yet, the performance of the calibration is highly dependent on this heuristic selection as well as the performance of the imaging methods.

Here, a calibration procedure to balance the power between each frequency is proposed by reliving the uncertainty of the fixed frequency selection of [3]. In this article, the improvement in calibration is achieved by comparing all possible calibration parameter sets at each frequency for the scattering parameter data. In addition, a weighting regularization for the TSVD is presented. In addition to offering better reconstructions, the proposed scheme also allows the automation of the imaging algorithms. A through-the-wall experiment with TSVD is utilized to test and show the performance of the proposed calibration technique.

II. IMAGING ALGORITHM

In this study, the TSVD method is applied for wideband scattering parameter data to solve the inverse scattering problem by reconstructing qualitative images. Under Born's approximation of the total internal field, the problem can be linearized by replacing the total internal field with the incident field as [31]

$$S_{m,n}=\frac{\mathrm{j}\omega\in_0}{2\alpha_m\alpha_n}\int\int_v\int\left(\boldsymbol{E}_{\boldsymbol{m}}^{\boldsymbol{inc}}\left(\boldsymbol{r}'\right)\cdot\ \boldsymbol{E}_{\boldsymbol{n}}^{\boldsymbol{inc}}\left(\boldsymbol{r}'\right)\right)\Delta\in\left(\boldsymbol{r}'\right)d\boldsymbol{r}' \tag{1}$$

where $S_{m,n}$ and $\boldsymbol{E}_{\boldsymbol{m(n)}}^{\boldsymbol{inc}}$ are the scattering portions of the scattering parameters and the incident field for the corresponding *m*th and *n*th antennas, respectively. The contrast is given with $\Delta\in(\boldsymbol{r}')=\in(\boldsymbol{r}')-\in_b(\boldsymbol{r}')$ while the dielectric permittivity of the object, the background, and the free space are denoted with $\in$, $\in_b$ and $\in_0$, respectively. The spatial coordinate $\boldsymbol{r}'$ stands for the points in the investigated region, while *V* is the volume of the object. The known root power at the *m*th and *n*th antenna ports is given with α, *j* is the imaginary unit, and ω is the angular frequency. The symbol (·) stands for dot product between two vectors. In the transverse magnetic (TM_z) configuration, the incident field for a line source becomes the Hankel function of zero-order first kind as

$$\boldsymbol{E}_{\boldsymbol{m(n)}}^{\boldsymbol{inc}}\left(\boldsymbol{r}'\right)=\frac{\mathrm{j}}{4}H_0^{(1)}\left(k_b\left|\boldsymbol{r}'-\boldsymbol{r}_{\boldsymbol{m(n)}}\right|\right) \tag{2}$$

where $k_b=\sqrt{\omega^2\in_b\mu_0}$ is the nonmagnetic background's wavenumber and μ_0 is the magnetic permeability of the free space. The positions of *m*th and *n*th ports are denoted with $\boldsymbol{r}_{\mathrm{m(n)}}$.

Next, the problem cast in (1) can also be given in a more compact form as

$$S_{m,n}=L\left\{\Delta\in\left(\boldsymbol{r}'\right)\right\} \tag{3}$$

where L is a linear integral operator taking into account the dot product operation and the coefficients defined in (1). To calculate the inverse of the operator L and find the unknown contrast, the TSVD method can be applied as

$$\Delta\in\left(\boldsymbol{r}'\right)=\sum_{T=T_1}^{T_D}\sum_{t=1}^{T}\sigma_t^{-1}\left\langle\mathbf{S},u_t\right\rangle v_t \tag{4}$$

where *u*, *v*, and σ are the left singular vectors, right singular vectors, and singular values in descending order of the singular value decomposition of the operator, $L\left(\mathrm{SVD}(L)=\left\langle u,\sigma,v\right\rangle\right)$ and $\mathbf{S}=[S_{\mathrm{m,n}}]_{\mathrm{M\times N}}$ (M and N denote the number of *m*th and *n*th antennas, respectively) is the bistatic scattering parameter matrix. To further improve the regularization of the TSVD method, we defined an interval for the truncation index *T* between the values T_1 and T_D. In proposed truncation, the higher singular values are weighted dominantly, while the lower singular values have less contribution to the calculation of $\Delta\in(\boldsymbol{r}')$. By doing so, a smooth truncation is applied. To define the truncation indices, first, singular values are converted to decibel values, and then the threshold limit is selected according to these logarithmic values, as shown in [32]. The contrast found in (4) is a complex vector, and to present a qualitative representation of the investigated region, the normalized indicator of the imaging algorithm is defined as

$$I\left(\boldsymbol{r}'\right)=\frac{\left|\Delta\in\left(\boldsymbol{r}'\right)\right|^2}{max\left(\left|\Delta\in\left(\boldsymbol{r}'\right)\right|^2\right)}. \tag{5}$$

III. CALIBRATION METHOD

Multi-static systems require calibration to resolve the mismatch between the inversion model and the measurement system because imaging algorithms cannot account for all aspects of physical measurement. Also, the inversion algorithms need the scattering portion of the measurements, which is approximately the difference between total and incident field measurements. This study involves 2 distinct total field measurements conducted under conditions of object presence and absence behind a wall. The first measurement ($S_{m,n}^{presence}$) consists of the incident field, the wall's contribution, and the scattering field from the object, while the other measurement ($S_{m,n}^{absence}$) contains the incident field and the wall's contribution. Therefore, the scattering portion can be calculated as $S_{m,n}=S_{m,n}^{presence}-S_{m,n}^{absence}$.

The multi-frequency multi-static inversion methods produce outcomes that are more robust and unambiguous in comparison to single-frequency mono/bi-static configurations [33, 34]. Even though the mismatch between scattered and total field measurements is resolved by using differential measurements, the given TSVD formulation may prove inadequate in practical experimental scenarios as it neglects the possibility of variations in power among excitations at different frequencies [3]. This is mostly caused by antenna radiation characteristics, and it is solved by making an additional measurement [30], and using a microwave imaging solution of an existing measurement [3]. Consequently, it is necessary to conduct a calibration procedure in order to equalize the power discrepancies among various frequencies. Before performing the measurements, hardware calibration is required to compensate for the errors stemming from components of the vector network analyzer, cables, and connectors. By doing so, the VNA plane is transferred to the port of the antennas.

To achieve this aim, the first step is to solve the inverse scattering problem $\Delta\in_f$ (see (4)) by using $S_{m,n}$ and $\boldsymbol{E}^{\boldsymbol{inc}}_{\boldsymbol{m(n)}}$ at every single frequency, $f_i = 1,2,\ldots N_f$, where N_f is the number of frequencies. Next, the parameters α_{f_i,f_j} are established to calibrate the input data, which is scattering parameters in this work, at the f_ith frequency with the power of the scattered field at the f_jth frequency, where $f_j = 1,2,\ldots N_f$ as

$$\alpha_{f_i,f_j} = \arg\min_{\beta} \sum_{p=1}^{P} \left| \Delta\in_{f_i}\left(\boldsymbol{r}_p^{'}\right) - \beta\Delta\in_{f_j}\left(\boldsymbol{r}_p^{'}\right) \right|^2 \tag{6}$$

where p stands for index number of sampled spatial coordinates $\boldsymbol{r}'$, and P is the maximum number of sampling points. Thus, the summation is performed over sampling points in the investigated region. Then, by setting the gradient to zero, the minimizer can be obtained as follows:

$$\alpha_{f_i,f_j} = \frac{\sum_{p=1}^{P} \Delta\in_{f_j}\left(\mathbf{r}_{\mathbf{p}}^{'}\right)\Delta\in_{f_i}\left(\mathbf{r}_{\mathbf{p}}^{'}\right)^*}{\sum_{p=1}^{P}\left|\Delta\in_{f_i}\left(\mathbf{r}_{\mathbf{p}}^{'}\right)\right|^2}. \tag{7}$$

Here, the parameter α_{f_i,f_j} has N_f by N_f values with having 1 at the diagonal elements when $f_i = f_j$ and it is formed as:

$$\alpha_{f_i,f_j} = \begin{bmatrix} 1 & \alpha_{1,2} & \alpha_{1,3} & \alpha_{1,4} & \alpha_{1,5} \\ \alpha_{2,1} & 1 & \alpha_{2,3} & \alpha_{2,4} & \alpha_{2,5} \\ \alpha_{3,1} & \alpha_{3,2} & 1 & \alpha_{3,4} & \alpha_{3,5} \\ \alpha_{4,1} & \alpha_{4,2} & \alpha_{4,3} & 1 & \alpha_{4,5} \\ \alpha_{5,1} & \alpha_{5,2} & \alpha_{5,3} & \alpha_{5,4} & 1 \end{bmatrix} \tag{8}$$

which gives us N_f set of possible N_f calibration parameters and one of these sets can be used to calibrate the measured data as in [3] (i.e. $f_j = N_f$)

$$\mathbf{S}^{\text{calibrated}} = \begin{bmatrix} \alpha_{1,5}\mathrm{S}^1_{m,n} \\ \alpha_{2,5}\mathrm{S}^2_{m,n} \\ \vdots \\ 1\mathrm{S}^{N_f}_{m,n} \end{bmatrix} \tag{9}$$

where superscript of $S_{m,n}$ denotes the frequency index. It should be noted that the variables $\mathbf{S}^{\text{calibrated}}$ and $\boldsymbol{E}^{\text{inc}}$ are arranged as taking into account all different frequency measurements (by concentrating all possible transmitting antenna, receiving antenna and frequency information) and it is employed to the (1). Here, the selection of f_j is heuristic.

However, the selection of value f_j highly impacts the result of the inversion algorithms and this selection cannot be foreseen. This necessity can be eliminated by balancing each set of α_{f_i,f_j} by minimizing

$$\begin{aligned} \alpha^{\text{imp}}_{f_i,f_j} &= \arg\min_{\beta} \sum_{d=1}^{N_f} \left| \alpha_{:,f_i}(d) - \beta\alpha_{:,f_j}(d) \right|^2 \\ &= \frac{\sum_{d=1}^{N_f} \alpha_{:,f_j}(d)\alpha_{:,f_i}(d)^*}{\sum_{d=1}^{N_f}\left|\alpha_{:,f_i}(d)\right|^2} \end{aligned} \tag{10}$$

where $\alpha^{\text{imp}}_{f_i,f_j}$ consists of N_f by N_f values having 1 when $f_i = f_j$ (has similar form as in (8)) and it presents more robust calibration than α_{f_i,f_j} since it takes into account all possible power differences at each operating frequency. Next, the final calibration parameter can be found as

$$\alpha^{\text{final}}_{f_j} = \frac{\sum_{f_i=1, f_i\neq f_j}^{N_f} \alpha^{\text{imp}}_{f_i,f_j}}{N_f - 1}. \tag{11}$$

Finally, the calibrated scattering parameter data can be defined as

$$\mathbf{S}^{\text{calibrated}} = \begin{bmatrix} \alpha_1^{\text{final}}\mathrm{S}^1_{m,n} \\ \alpha_2^{\text{final}}\mathrm{S}^2_{m,n} \\ \vdots \\ \alpha_{N_f}^{\text{final}}\mathrm{S}^{N_f}_{m,n} \end{bmatrix}. \tag{12}$$

In addition to providing better reconstructions, using $\alpha^{\text{final}}_{f_j}$ also allows automation of the calibration process by removing the ambiguity of the selection of f_j.

IV. THROUGH-THE-WALL EXPERIMENT

In this experiment, the measurements are performed in a non-anechoic environment for a TWI configuration. Note that the imaging setup is used to verify the proposed calibration method. In order to achieve the intended objective, a metallic cylindrical bar is positioned at the rear of the wall. Subsequently, a Rohde & Schwarz ZNBT8 model vector network analyzer is situated on the opposite side of the wall. This analyzer has the capacity to measure S-parameters using 8 ports. The antenna array consists of 8 Vivaldi antennas that are identical, and these antennas are arranged linearly in a straight line with an equal separation between each antenna. The frequency of operation is swept in a linear manner within the range of 2.2–2.6 GHz, with a step size of 0.1 GHz. As a result, a total of 5 distinct frequencies ($N_f = 5$) are selected for the purpose of measurements. The network analyzer's IF bandwidth is consistently 100 Hz for each discrete frequency measurement. The pictures of this experiment are given in Fig. 1a and b, and more details about the measurement setup can be obtained from [3].

The TSVD thresholds T_1 and T_D correspond to a singular value index; however, they are decided by assigning a decibel value to the singular values σ. For this particular experiment, the decibel lower and

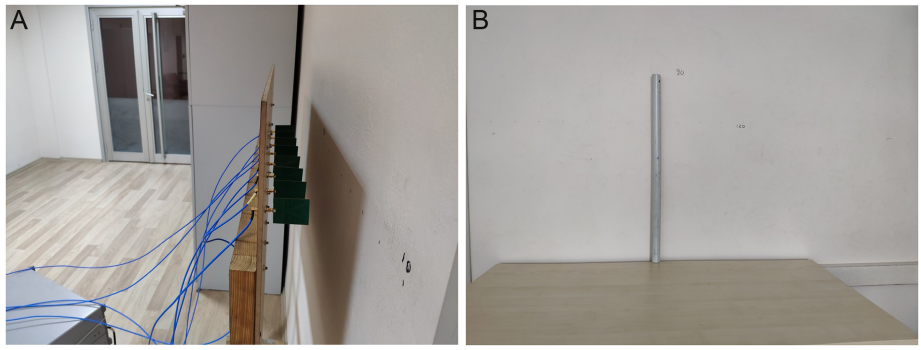

Fig. 1. Photographs of the through the wall imaging setup. (a) Eight identical Vivaldi antennas are employed for transmitting and receiving and connected to an eight-port vector network analyzer. (b) A metallic bar is placed behind the wall above a table. These photographs are taken from [3].

upper limits are −7 and −13 dB, respectively. The threshold scanning step is −2 dB. The index values are selected by finding the closest decibel values to the given thresholds. For this particular experiment, these index values are 37, 90, 95, and 115 for each threshold *T*. The total number of singular values is computed by multiplying the number of transmitters, receivers, and frequencies, which results in 980. The distribution of singular values is given in Fig. 2 for the values $20\log(\sigma/\sigma_{max})$.

First, the TSVD method is applied to the calibrated data (see (9) for corresponding f_j) with α_{f_i,f_j} at each calibrated operating frequency $f_{cal}=2.2$, 2.3, 2.4, 2.5, and 2.6 GHz. The results of the TSVD indicator, (see (5)) are illustrated in Fig. 3a–e for each f_{cal} value. It is observed that the indicator when $f_{cal}=2.2$ GHz (see Fig. 3a), provides good structural properties of the object with very noisy reconstructions in general. When $f_{cal}=2.3$ GHz (see Fig. 3b), the size of the object shrinks, but noise is more suppressed. The noise begins to increase when $f_{cal}=2.4$ GHz (see Fig. 3c), and the size of the object begins to expand when $f_{cal}=2.5$ GHz (see Fig. 3d). The indicator presents reasonably good structural properties and less noisy images at $f_{cal}=2.6$ GHz (see Fig. 3e). Next, the TSVD method is employed with the data calibrated (see (12)) using $\alpha_{f_j}^{final}$ and the indicator is depicted in Fig. 3f. It can be seen that the size of the object is perfectly retrieved. The background artifacts, commonly referred to as noise, exhibit a generally low level in the imaging process; however, it is observed that the noise level is comparatively larger when the calibration frequencies are set to $f_{cal}=2.3$ GHz and $f_{cal}=2.6$ GHz.

To compare the results of the proposed calibration method, the calibration method in [3] and without power balancing calibration, a quantitative criterion is calculated using the Dice similarity coefficient [35]. To this aim, the indicators depicted in Fig. 3 are converted to binary images using the threshold values between 0.05 and 0.95 with a 0.05 increment. The process of obtaining binary values involves assigning a value of 1 to normalized reconstruction *I* if it exceeds the chosen threshold and a value of 0 if it falls below the threshold. The actual image is obtained by assigning 1 to the object's position and 0 to other points in the image. The Dice similarity coefficient (DSC) is defined as

$$\mathrm{DSC}(\%)=100\times\frac{2\left(U_{CP}/U_{UP}\right)}{1+\left(U_{CP}/U_{UP}\right)} \tag{11}$$

where the variable U_{UP} represents the number of points that are equivalent to 1 in both the actual binary image and the reconstructed binary image. Similarly, U_{CP} denotes the number of points that are equivalent to 1 in solely the actual binary image and the reconstructed binary image. The percentage DSC values are plotted

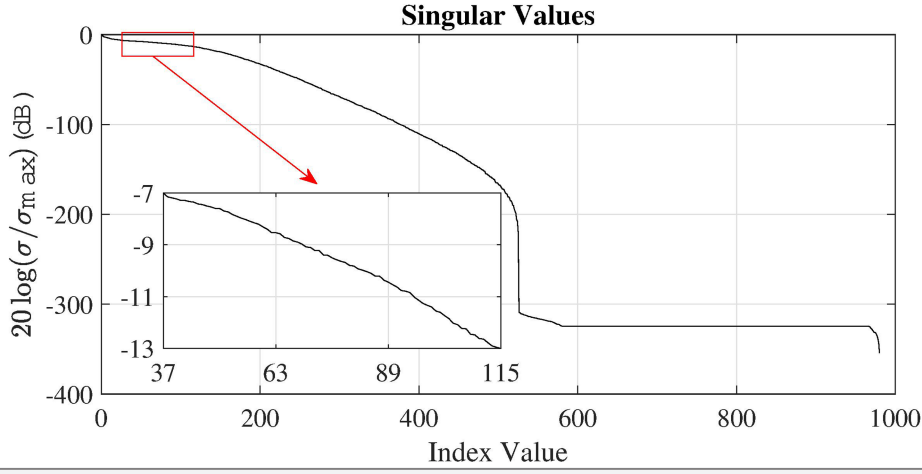

Fig. 2. The normalized singular value distribution.

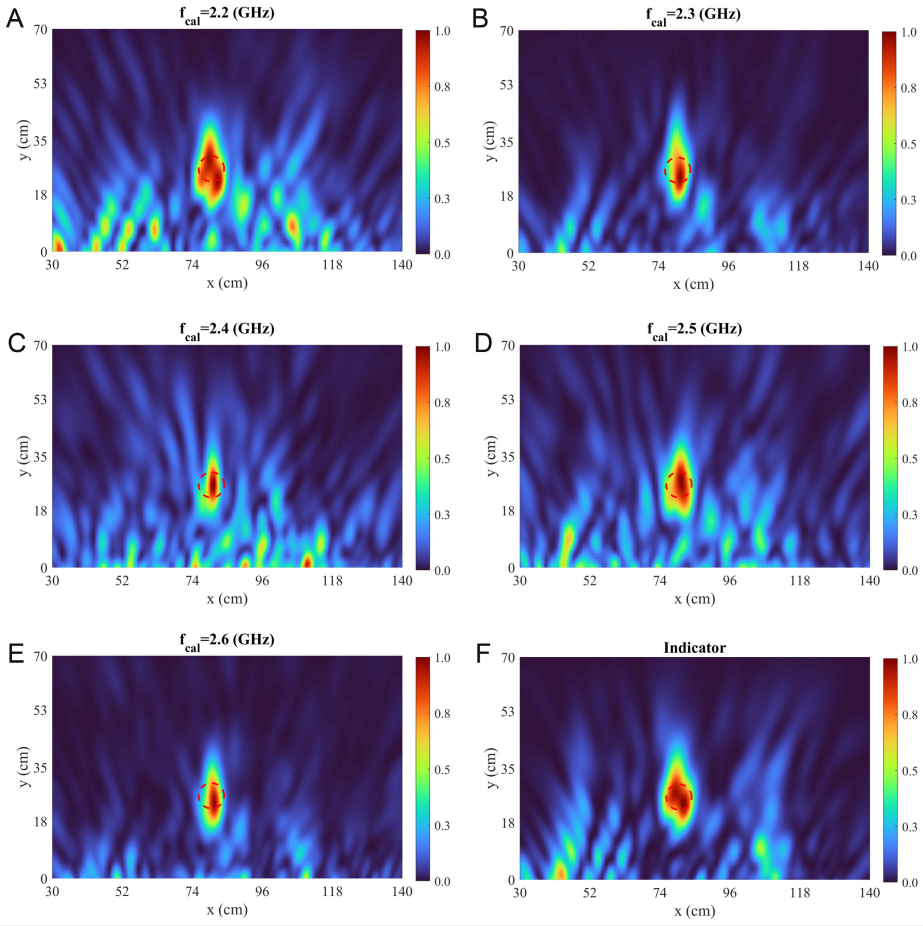

Fig. 3. The truncated singular value decomposition indicators when (a) f_{cal} = 2.2, (b) f_{cal} = 2.3, (c) f_{cal} = 2.4, (d) f_{cal} = 2.5, (e) f_{cal} = 2.6 GHz and (f) with using the proposed calibration method.

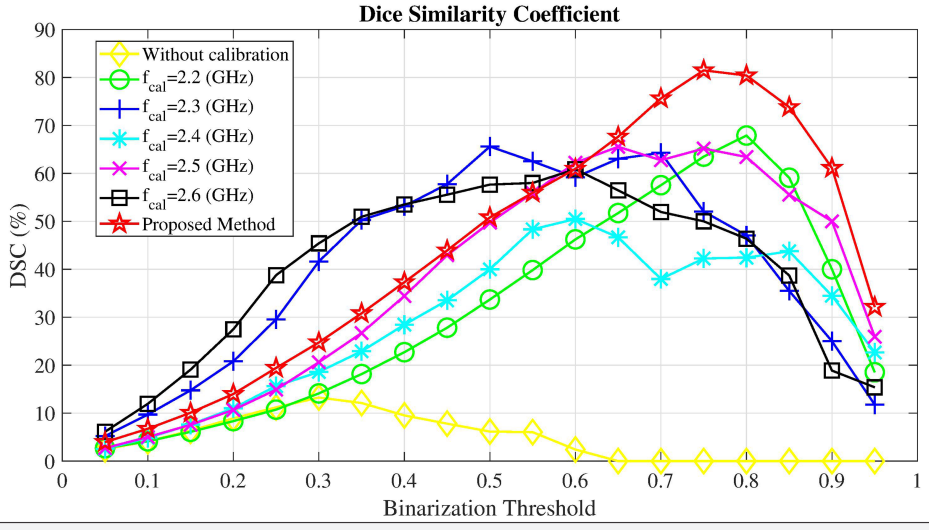

Fig. 4. The Dice similarity coefficient for the binary images of truncated singular value decomposition indicators presented in Fig. 3a–f and the result without applying any kind of power balancing. The binarization threshold values are between 0.05 and 0.95 with a 0.05 increment.

in Fig. 4 for the quantitative analysis. It can be seen that the proposed method provides the best reconstructions when the threshold goes above 0.6. The binary indicators acquired using the proposed calibration method when $f_{cal}=2.2$ GHz and $f_{cal}=2.4$ GHz are given in Fig. 5A-C for the binarization threshold of 0.75. These f_{cal} values are selected for visualization because they have the highest DSC values for the chosen binarization threshold. It can be seen that the proposed method provides very high accuracy for the shape of the object and the background's noise level.

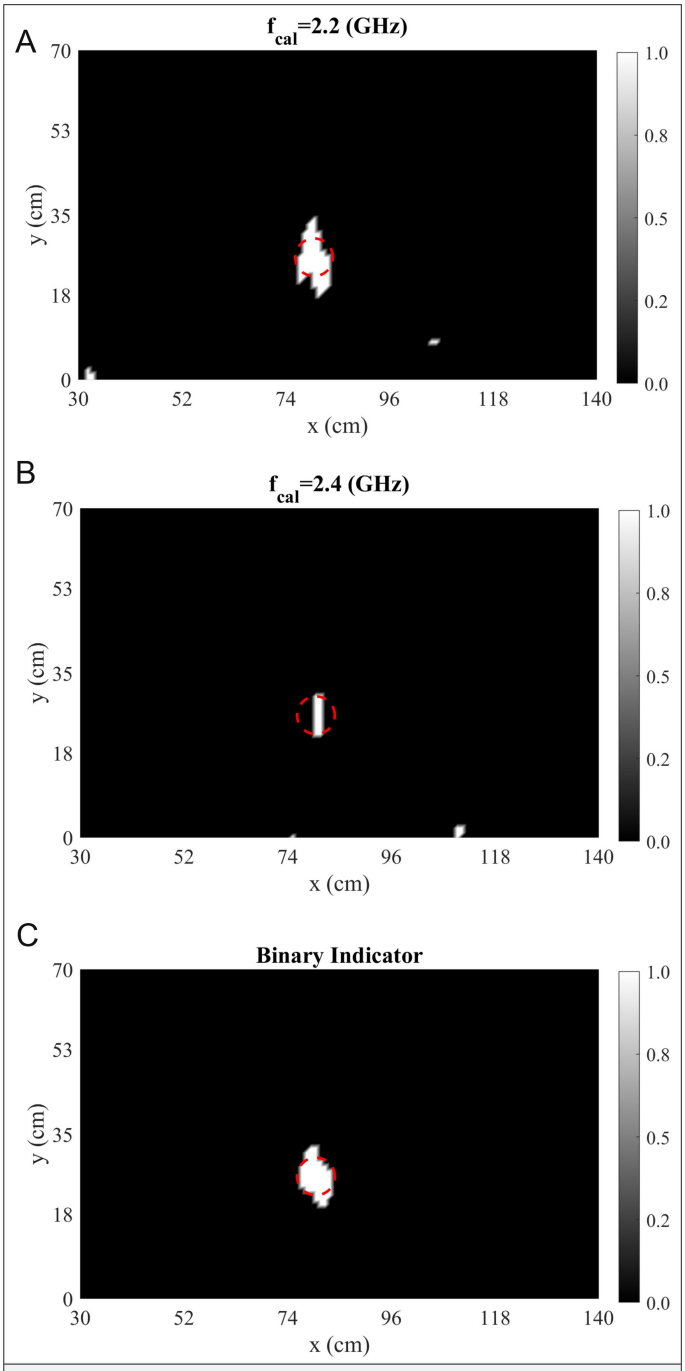

Fig. 5. The binary truncated singular value decomposition indicators when (a) $f_{cal}=2.2$, (b) $f_{cal}=2.4$ GHz, and (c) with using the proposed calibration method.

V. CONCLUSION

For wide-band measurement systems, this work has proposed a calibration method to balance the power differences at each distinct frequency measurement. Enhancement of the calibration is attained through the comparison of all feasible calibration parameter sets for every constant frequency and subsequently exhibiting solely one calibration parameter set for the scattering parameter data. The proposed scheme not only provides superior reconstructions but also facilitates the automation of imaging algorithms by resolving heuristic selection. Here, the proposed calibration method is verified with an experimental TWI application at microwave frequencies.

Peer-review: Externally peer-reviewed.

Declaration of Interests: The author has no conflict of interest to declare.

Funding: The author declared that this study has received no financial support.

REFERENCES

1. N. K. Nikolova, *Introduction to Microwave Imaging*. Cambridge, United Kingdom: Springer Science & Business Media, 2017.
2. Z. Zheng *et al.*, "Recovering human pose and shape from through-the-wall radar images," *IEEE Trans. Geosci. Remote Sens.*, vol. 60, pp. 1–15, 2022. [CrossRef]
3. S. Dogu, M. N. Akıncı, M. Cayoren, and İ. Akduman, "Truncated singular value decomposition for through-the-wall microwave imaging application," *IET Microw. Antennas Propag.*, vol. 14, no. 4, pp. 260–267, 2020. [CrossRef]
4. R. Cicchetti, S. Pisa, E. Piuzzi, E. Pittella, P. D'Atanasio, and O. Testa, "Numerical and experimental comparison among a new hybrid ft-music technique and existing algorithms for through-thewall radar imaging," *IEEE Trans. Microw. Theor. Techn.*, vol. 69, no. 7, pp. 3372–3387, 2021. [CrossRef]
5. F. Soldovieri, and R. Solimene, "Through-wall imaging via a linear inverse scattering algorithm," *IEEE Geosci. Remote Sens. Lett.*, vol. 4, no. 4, pp. 513–517, 2007. [CrossRef]
6. I. Akduman, L. Crocco, and F. Soldovieri, "Experimental validation of a simple system for through-the-wall inverse scattering," *IEEE Geosci. Remote Sens. Lett.*, vol. 8, no. 2, pp. 258–262, 2011. [CrossRef]
7. S. Costanzo, G. Lopez, and G. D. Massa, "Spatial domain indirect holography for a full phaseless approach to biomedical microwave imaging," *IEEE Open J. Antennas Propag.*, vol. 3, pp. 604–612, 2022. [CrossRef]
8. S. Dogu, H. Onal, T. Yılmaz, I. Akduman, and M. N. Akıncı, "Continuous monitoring of hyperthermia treatment of breast tumors with singular sources method," *IEEE Access*, vol. 11, pp. 6584–6593, 2023. [CrossRef]
9. K. Bakian-Dogaheh, Y. Fang, and M. Moghaddam, "A quad-band near-field antenna array for a multistatic microwave imaging chamber," *IEEE Antennas Wirel. Propag. Lett.*, pp. 1–5, 2023.
10. İ. Dilman *et al.*, "Monitoring of intracerebral hemorrhage with a linear microwave imaging algorithm," *Med. Biol. Eng. Comput.*, vol. 61, no. 1, pp. 33–43, 2023. [CrossRef]
11. W. Shao, and T. McCollough, "Advances in microwave near-field imaging: Prototypes, systems, and applications," *IEEE Microw. Mag.*, vol. 21, no. 5, pp. 94–119, 2020. [CrossRef]
12. S. Takahashi, K. Suzuki, T. Hanabusa, and S. Kidera, "Microwave subsurface imaging method by incorporating radar and tomographic approaches," *IEEE Trans. Antennas Propag.*, vol. 70, no. 11, pp. 11009–11023, 2022.
13. S. Dogu, M. N. Akıncı, and E. Gose, "Experimental moving target imaging in a nonanechoic environment with linear sampling method," *IEEE Geosci. Remote Sens. Lett.*, vol. 18, no. 3, pp. 441–445, 2021. [CrossRef]
14. S. Dogu, D. Tajik, M. N. Akıncı, and N. K. Nikolova, "Improving the accuracy of range migration in 3-d near-field microwave imaging," *IEEE Trans. Microw. Theor. Techn.*, pp. 1–12, 2023.
15. Y. Meng, C. Lin, A. Qing, and N. K. Nikolova, "Accelerated holographic imaging with range stacking for linear frequency modulation radar,"

IEEE Trans. Microw. Theor. Techn., vol. 70, no. 3, pp. 1630–1638, 2022. [CrossRef]
16. W. C. Chew, and Y. M. Wang, "Reconstruction of twodimensional permittivity distribution using the distorted born iterative method," *IEEE Trans. Med. Imag.*, vol. 9, no. 2, pp. 218–225, 1990. [CrossRef]
17. D. Tajik, R. Kazemivala, and N. K. Nikolova, "Real-time imaging with simultaneous use of born and rytov approximations in quantitative microwave holography," *IEEE Trans. Microw. Theor. Techn.*, vol. 70, no. 3, pp. 1896–1909, 2022. [CrossRef]
18. D. Colton, H. Haddar, and M. Piana, "The linear sampling method in inverse electromagnetic scattering theory," *Inverse Probl.*, vol. 19, no. 6, S105–S137, 2003. [CrossRef]
19. M. N. Akıncı, "Improving near-field orthogonality sampling method for qualitative microwave imaging," *IEEE Trans. Antennas Propag.*, vol. 66, no. 10, pp. 5475–5484, 2018. [CrossRef]
20. W.-K. Park, "On the application of orthogonality sampling method for object detection in microwave imaging," *IEEE Trans. Antennas Propag.*, vol. 71, no. 1, pp. 934–946, 2023. [CrossRef]
21. D. O. Rodriguez-Duarte *et al.*, "Experimental validation of a microwave system for brain stroke 3-d imaging," *Diagnostics*, vol. 11, no. 7, 2021. [CrossRef]
22. Y. Huang, Y. Zha, Y. Wang, and J. Yang, "Forward looking radar imaging by truncated singular value decomposition and its application for adverse weather aircraft landing," *Sensors (Basel)*, vol. 15, no. 6, pp. 14397–14414, 2015. [CrossRef], pp. 14.
23. F. Soldovieri, and R. Persico, "Reconstruction of an embedded slab from multifrequency scattered field data under the distorted Born approximation," *IEEE. Trans. Antennas Propag.*, vol. 52, no. 9, pp. 2348–2356, 2004. [CrossRef]
24. L. Ji, Q. Guo, and M. Zhang, "Medical image denoising based on biquadratic polynomial with minimum error constraints and low-rank approximation," *IEEE Access*, vol. 8, pp. 84950–84960, 2020. [CrossRef]
25. W. Ha, and C. Shin, "Seismic random noise attenuation in the laplace domain using singular value decomposition," *IEEE Access*, vol. 9, pp. 62029–62037, 2021. [CrossRef]
26. C. Gilmore, I. Jeffrey, M. Asefi, N. T. Geddert, K. G. Brown, and J. Lovetri, "Phaseless parametric inversion for system calibration and obtaining prior information,", *IEEE Access*, vol. 7, pp. 128735–128745, 2019. [CrossRef]
27. D. O. Rodriguez-Duarte, J. A. Tobon Vasquez, and F. Vipiana, "Hybrid simulation-measurement calibration technique for microwave imaging systems," in 2021 15th European Conference on Antennas and Propagation (EuCAP), pp. 1–5, 2021. [CrossRef]
28. D. O. Rodriguez-Duarte, J. A. T. Vasquez, and F. Vipiana, "Multi-shot calibration technique for microwave imaging systems," in 2021 IEEE Conference on Antenna Measurements & Applications (CAMA), pp. 476–480, 2021. [CrossRef]
29. D. O. Rodriguez-Duarte, C. Origlia, J. A. T. Vasquez, R. Scapaticci, L. Crocco, and F. Vipiana, "Experimental assessment of real-time brain stroke monitoring via a microwave imaging scanner," *IEEE Open J. Antennas Propag.*, vol. 3, pp. 824–835, 2022. [CrossRef]
30. R. Solimene, F. Soldovieri, A. Baratonia, and R. Pierri, "Experimental validation of a linear inverse scattering twi algorithm by a sf-cw radar," *IEEE Antennas Wirel. Propag. Lett.*, vol. 9, pp. 506–509, 2010. [CrossRef]
31. A. S. Beaverstone, D. S. Shumakov, and N. K. Nikolova, "Frequency-domain integral equations of scattering for complex scalar responses," *IEEE Trans. Microw. Theor. Techn.*, vol. 65, no. 4, pp. 1120–1132, 2017. [CrossRef]
32. I. Sarwar *et al.*, "Low-cost low-power acceleration of a microwave imaging algorithm for brain stroke monitoring," *J. Low Power Electron. Appl.*, vol. 8, no. 4, 2018. [CrossRef]
33. H. Sato, and S. Kidera, "Noise-Robust Microwave Breast Imaging Applied to Multi-Frequency Contrast Source Inversion," *IEEE J. Electromagn., RF, Microw., Med. Biol.*, vol. 5, no. 2, pp. 187–193, 2021.
34. L. Wang, "Multi-frequency holographic microwave imaging for breast lesion detection," *IEEE Access*, vol. 7, p. 83, 984–983, 993, 2019.
35. L. R. Dice, "Measures of the amount of ecologic association between species," *Ecology*, vol. 26, no. 3, pp. 297–302, 1945. [CrossRef]

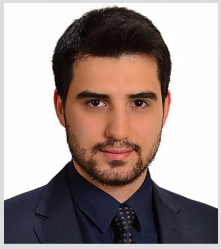

Semih Doğu received the B.S. degree in electrical engineering and electronics and communication engineering from Yildiz Technical University, Istanbul, Turkey, in 2015 and 2016 respectively, and the M.S. degree in telecommunication engineering from Istanbul Technical University, Istanbul, Turkey, in 2017, and the Ph.D. degree from the Istanbul Technical University, Istanbul, Turkey, in 2023. He is also a Research Assistant and a Teaching Assistant with the Department of Electronics and Communication Engineering, Istanbul Technical University. From 2021 to 2022, he was a Visiting Researcher of electrical engineering at McMaster University, Hamilton, ON, Canada. His current research interests include electromagnetic scattering problems, imaging methods for noninvasive diagnostics through the wall radar, and microwave biomedical imaging. He was a recipient of the 2016 IEEE Antennas and Propagation Ulrich L. Rohde Innovative Conference Paper Award on Antenna Measurements and Applications and he was a recipient of the Leopold B. Felsen Excellence in Electromagnetics award.